Self-assembled calcium phosphate nanocomposites using block copolypeptide templates†

Yan-Yan Hu,‡[ab] Yusuf Yusufoglu,‡[ab] Mathumai Kanapathipillai,[b] Chu-Ya Yang,[c] YaQiao Wu,[b] Papannan Thiyagarajan,[d] Timothy Deming,[c] Mufit Akinc,[b] Klaus Schmidt-Rohr[b] and Surya Mallapragada*[a]

Received 4th March 2009, Accepted 4th August 2009
First published as an Advance Article on the web 9th September 2009
DOI: 10.1039/b904440j

Polylysine and polyleucine based block copolypeptides ($K_{170}L_{30}$) that form gels at very low concentrations in aqueous media are used as templates for forming self-assembled calcium phosphate nanocomposites. The synthesis method allows for simultaneous formation of the self-assembled block copolypeptide gel and of the inorganic phase, providing inorganic contents of over 50 wt% in the nanocomposite, approaching the inorganic content in bone. The self-assembled nanocomposites are characterized by thermogravimetric analysis, X-ray diffraction (XRD), Fourier transform infrared (FTIR) spectroscopy, solid state nuclear magnetic resonance (NMR), transmission electron microscopy (TEM) and small angle X-ray scattering (SAXS). The nanocomposites formed in the presence of the block copolypeptide templates exhibit very different nanoparticle morphologies than those formed in the absence of the organic phase. Multinuclear solid state NMR methods are used to prove nanocomposite formation and characterize the secondary structure and mobility of the block copolypeptide template. The data from XRD, FTIR, and ^{31}P NMR consistently show that the inorganic phase present in the nanocomposite is carbonated hydroxyapatite of nano-scale dimensions, with an elongated plate-like morphology, observed by TEM and SAXS, similar to the mineral phase of natural bone. Overall, this approach allows a bioinspired bottom-up approach to self-assembled hydroxyapatite nanocomposites using block copolypeptide templates, which could have applications in tissue repair.

Introduction

In biological systems, calcium phosphate ceramics are the most important inorganic components of hard tissues, and synthetic substitutes have been used in medicine and dentistry for more than 20 years.[1] Among the six principal calcium salts of orthophosphoric acid, hydroxyapatite (HAp: $Ca_{10}(PO_4)_6(OH)_2$) is the best known because of its compositional and biological similarities to the mineral phase of human bone. For instance, apatite in the form of carbonated hydroxide-deficient hydroxyapatite (CO_3HAp) including a variety of other minor dopants is present in natural bone to impart stiffness and hardness.[1,2] It accounts for approximately 65 wt% of total bone mass with the remaining being mainly collagen and water.[3,4] In bone formation, biomineralization produces a nanocomposite with layers of collagen molecules alternating with thin and elongated nanocrystals of carbonated apatite,[5] in a process involving more than 200 different proteins.[6] These proteins act as inhibitors and nucleators for the growth of apatite nanocrystals, anchored to the collagen.[5,7] The combination of inorganic and organic components provides increased toughness compared to HAp alone.[8,9] As a result, biomaterials such as bone as well as dentine in teeth, in which the organic matrix acts as a guide and imparts toughness to the otherwise brittle inorganic phase, have attracted the interest of researchers into the investigation and development of novel organic–inorganic biocomposite materials suitable for prosthetic medical applications.[8,10]

Biocomposites of HAp in conjunction with various synthetic polymers[11–16] and natural polymers such as collagen,[17–20] chitosan,[8,21–23] cellulose[24–26] and gelatin[4,27,28] have been investigated extensively. We have shown successful templating of calcium phosphates by self-assembling thermo-reversible cationic and Pluronic block-copolymer gels with 15 wt% inorganic content.[29] This method enabled the formation of self-assembled nanocomposites from solution by changing the temperature. Subsequently, self-assembling thermo-reversibly gelling anionic and zwitterionic pentablock copolymers conjugated to hydroxyapatite nucleating peptides were used as templates for precipitation of calcium phosphate nanostructures.[30] The inorganic fraction of the nanocomposites was increased to about 30–40 wt%.[31] The inorganic content in these nanocomposites was still significantly lower than that seen in nature (65 wt%). The high polymer concentrations (~25 wt%) needed for gel formation in these block copolymer systems is one limitation to increasing the weight fraction of the inorganic phase using these synthetic block copolymer templates. Besides our group, other researchers using

[a]*Ames Laboratory and Iowa State University, 3035 Sweeney Hall, Ames, IA, 50011-2230, USA. E-mail: suryakm@iastate.edu*
[b]*Ames Laboratory, Ames, IA, 50011, USA*
[c]*Department of Bioengineering, University of California, Los Angeles, CA, 90095, USA*
[d]*Advanced Photon Source, Argonne National Laboratory, 9700 S. Cass Ave, Argonne, IL, 60439, USA*

† Electronic supplementary information (ESI) available: ^{31}P NMR results. See DOI: 10.1039/b904440j

‡ Both authors contributed equally to the work.

similar *in-situ* synthesis methods also obtained polymer–HAp composites, but with relatively low inorganic content. For instance, Spanos and co-workers[13] synthesized a novel composite containing 9 wt% of HAp and 91 wt% of polymer (sulfonated polysulfone), while Wang and co-workers recently fabricated nanostructured HAp in the matrix of alginate with a maximum 30 wt% HAp exhibiting microstructures similar to natural bone.[32] The Liou group produced a poly(acrylic acid)-HAp nanocomposite of 30–32 wt% phosphate.[33]

In contrast, the Deming group has synthesized a family of novel block copolypeptides that form gels at very low concentrations (~0.5 wt%) and can serve as templates for biomineralization.[34–37] This paper investigates the use of these block copolypeptides as templates for forming self-assembled calcium phosphate nanocomposites to increase the inorganic content of the nanocomposite. We demonstrate the formation of HAp/block copolypeptide ($K_{170}L_{30}$) polymer nanocomposites with a maximum inorganic content of approximately 53 wt%. This approach is similar to nature where protein templates commonly control the nucleation and growth of the inorganic nanocrystalline phase in biomaterials such as bone.

Wet-chemical methods lend themselves to the formation of calcium phosphate ceramics with good crystallinity, physiological stability, and morphological characteristics resembling those of hard tissues.[38] A number of papers have described different wet-chemical methods including chelate[39–41] or urea decomposition,[42–44] precipitation,[38,45–48] and hydrolysis of calcium phosphate precursors.[49–52] In the present study, we used precipitation onto the self-assembling block copolypeptide templates to obtain polymer–inorganic hydrogel composites. Compared to other methods, this is a relatively simple technique utilizing mild experimental conditions that preclude polymer degradation. The resulting nanocomposites have been characterized by X-ray diffraction, ^{31}P NMR, Fourier-transform infrared spectroscopy, and high-resolution transmission electron microscopy (HRTEM) to identify the phosphate phase(s) formed; by ^{1}H and ^{31}P spin-diffusion NMR to prove nanocomposite formation; by TEM and small-angle X-ray scattering to determine the shape of the crystallites; and by ^{13}C NMR to determine the secondary structure and mobility of the polypeptide matrix. We believe that this work may contribute towards understanding the fundamental mechanism of biomineralization that is essential for the development of novel bioinspired materials for hard tissue repair and regeneration.

Results and discussion

The polylysine segment length was determined using GPC/LS, and ^{1}H NMR was used to determine the copolymer composition. Combined, these data showed that a block copolypeptide of $K_{170}L_{30}$ with low polydispersity was obtained. The consumption of the monomer and the formation of amide bonds from the polypeptide backbones (1650 cm^{-1}, 1540 cm^{-1}) was confirmed using FTIR measurements. ^{1}H NMR in deuterated TFA (d-TFA) indicated a 97%–98% removal of benzyloxycarbonyl groups from lysine residues.

The XRD patterns of the pure polymer (a), as-prepared HAp-polymer hydrogel (b), vacuum dried HAp/polymer composite (c), washed sample (after vacuum drying) (d), calcined sample (after TGA) (e), and pure HAp (Standard Reference Material® 2910) (f) are shown in Fig. 1. XRD patterns of pure polymer and pure HAp (Standard Reference Material® 2910) are included in the XRD Fig. 1 to compare with that of the nanocomposite sample. For pure polymer (Fig.1a), two broad humps were observed at about $2\Theta = 12°$ and 22° indicative of the amorphous nature of the polymer. The 12° peak might be attributed to rod–rod packing of helical polyleucine chains. All diffraction peaks of as-prepared composite hydrogel (Fig 1b) were matched to those of pure HAp (Fig 1f) and the ICDD standard card (JCPDS 9-432). The results are also in accordance with the calcium phosphate pH–concentration diagram[53] and experimentally shown by Yusufoglu and Akinc[41] that the most stable calcium phosphate phase is HAp at pH >6. Furthermore, the broadening and overlap of the peaks (broad peak at $2\Theta \approx 31°$ is a summed contributions of the (211), (112) and (300) planes of HAp) is a sign of small size or/and poor crystallinity of HAp crystals in the hydrogel sample. However, the crystallographic structure of HAp observed in the as-prepared HAp–polymer hydrogel is very similar to natural bone mineral and human dentine.[6,54,55] It is also worth noting that the as-prepared nanocomposite hydrogel shows a higher $I_{(002)}/I_{(211)}$ than that of pure HAp, indicating the preferential elongation of the crystals along the c-axis. Moreover, in addition to the characteristic HAp peaks, the XRD pattern of vacuum dried sample displayed some additional diffraction peaks belonging to ammonium nitrate (JCPDS 1-0809 and 76-2276) marked by solid circles in Fig.1c. Further, the sharp peak at $2\Theta = 29.45°$ matches well with the most intense peak of ammonium sodium nitrate (JCPDS

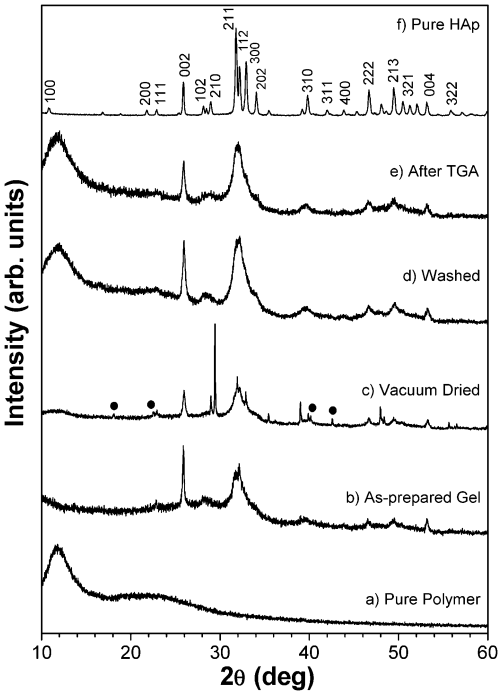

Fig. 1 X-ray diffraction patterns of (a) pure polymer, (b) as-prepared calcium phosphate/hydrogel nanocomposite, (c) vacuum dried nanocomposite, (d) washed sample (after vacuum drying), (e) calcined sample after TGA experiments and (f) pure HAp (Standard Reference Material® 2910).

28-0490). After washing the vacuum dried sample with deionized water, all diffraction peaks belonging to ammonium (sodium) nitrate disappeared (Fig.1d) and left only HAp peaks. In addition, it is also worth noting that HAp is the only phase present after TGA experiments as shown in Fig.1e.

FTIR spectroscopic characterization of the nanocomposites

The FTIR spectra of the pure polymer (a), vacuum dried nanocomposite (b), washed sample (after vacuum drying) (c) and pure HAp (Standard Reference Material® 2910) (d) are shown in Fig. 2. The FTIR spectrum of pure HAp (Fig. 2d) illustrates all the characteristic bands of stoichiometric HAp.[38,42] As expected, the spectrum of pure HAp exhibits phosphate peaks at 965 cm^{-1} (a single intense band), 470 cm^{-1}, between 1050–1095 cm^{-1} and 565, 602, 635 cm^{-1} (three sites) for ν_1, ν_2, ν_3 and ν_4 respectively.

The FTIR spectrum of pure polymer is shown in Fig. 2a. The possible assignments of all absorption peaks in Fig. 2 are provided in Table 1. Furthermore, the FTIR spectrum of vacuum dried HAp/polypeptide nanocomposite can be seen in Fig. 2b. The absorption bands at 566–601 cm^{-1}, 962 cm^{-1} and 1040–1100 cm^{-1} are associated with the phosphate groups of HAp. Moreover, the peaks at 1380 cm^{-1} and 832 cm^{-1} are assigned to nitrate groups, which is consistent with the results obtained from XRD. It is well established that for nitrate groups, the first absorption (at 1380 cm^{-1}) is intense and broad, and the second (at 840 cm^{-1}) has medium intensity and is narrow.[56] As illustrated in Fig. 2c, the peaks associated with nitrate groups disappeared in the FTIR spectrum of the washed sample. This implies that washing of the vacuum dried HAp/polymer composite removed nitrate species, consistent with the XRD results. As seen in the FTIR spectrum of the washed sample, in addition to the characteristic HAp absorption bands, the weak features arising from the vibrational modes of the carbonate were also observed at 873, 1415 cm^{-1} and 1462 cm^{-1},[50,57] suggesting

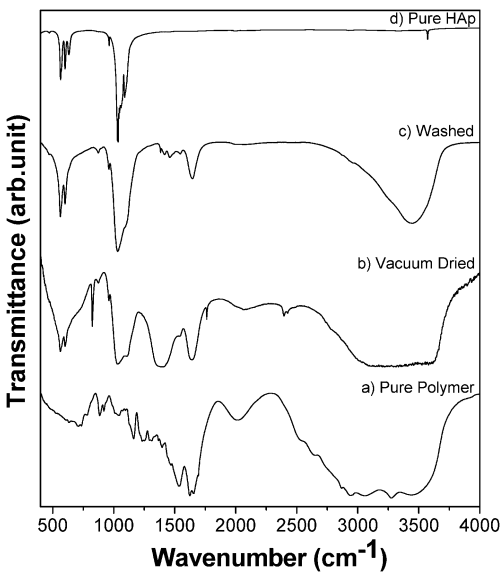

Fig. 2 FTIR spectra of the (a) pure polymer, (b) vacuum dried HAp/polypeptide hydrogel nanocomposite, (c) washed sample (after vacuum drying), and (d) pure HAp (Standard Reference Material® 2910).

Table 1 The possible assignments of FTIR peaks present in Fig. 2 (ref. 23,56,60,61,77–80)

Group Frequency (cm^{-1})	Assignment
3570	Hydroxyl stretching
3450 (broad)/1640	Water absorption bands
3350	N–H stretching of amine groups
3280	N–H stretching of amide I
2970/2850	C–H stretching
2050	$-NH_3^+$ bending mode
1630	Amide I mainly CO group stretching mode
1537	Amide II mainly N–H bend and C–N stretch
1470/730	C–H bending and methylene rocking
1390	Methyl C–H bend
1380/832	Nitrate groups
1350	Methyne C–H vibrations
1300	CH_2 deformation and wagging
1250	Amide III mainly C–N stretch and N–H in-plane deformation
1160	C–N stretch of amine groups
1080/700	C–C vibrations
873/1415/1462	Carbonate $\nu_2/\nu_{3a}/\nu_{3b}$ (for B–CO_3HAp)
566–601/962/1040–1100	Phosphate bands of HAp

that the HAp contains carbonate ions. While the CO_3^{2-} ions can replace OH^- (A-type substitution) or PO_4^{3-} (B-type substitution) in the HAp structure, the CO_3^{2-} peaks shown in Fig. 2c are assigned only to the B-type substitution (CO_3^{2-} ions replaces PO_4^{3-}).[50] The CO_3^{2-} substitution at the PO_4^{3-} site in HAp crystals is commonly observed for preparation in aqueous systems,[58] as has been also observed in the present work. As the apatite in human bone also contains CO_3^{2-} ions at about 4–8 wt% depending upon age, its presence in the HAp structure is beneficial.[6,59] It has been reported that at low concentration, CO_3^{2-} ions substantially improve the mechanical strength of apatite[59] and the presence of CO_3^{2-} ions in the HAp structure also influences the decomposition, sinterability, solubility and biological reactivity of the apatite.[47] Since no carbonate source was present in the starting materials, carbonate incorporation into the HAp might be due to the atmospheric carbon dioxide as has been observed during mineral precipitation in carbonate-free solutions.[25,60] Further, broad absorption bands centered around 3450 and 1640 cm^{-1} are due to incorporated water molecules,[53,61] which might also be present in Fig. 2a and 2b along with the polymer related peaks in the same spectral region.

The TGA results of as-prepared HAp/polypeptide hydrogel, vacuum dried HAp/polypeptide nanocomposite, washed sample and pure HAp (Standard Reference Material® 2910) are illustrated in Fig. 3. As can be seen from the trace of as-prepared HAp/polypeptide hydrogel, there is a sharp weight decrease between 70 and 175 °C, which is assigned to the loss of free and bound water. After vacuum drying, most of the water is removed (Fig. 3b). The weight loss in the 200–450 °C range is due to thermal decomposition of polymer and perhaps ammonium nitrate (as shown in Fig. 3c, weight loss between 200 and 450 °C is decreased for washed sample after removing ammonium nitrate). There is no change in sample weight above 500 °C, indicating that the polymer and nitrate species have decomposed

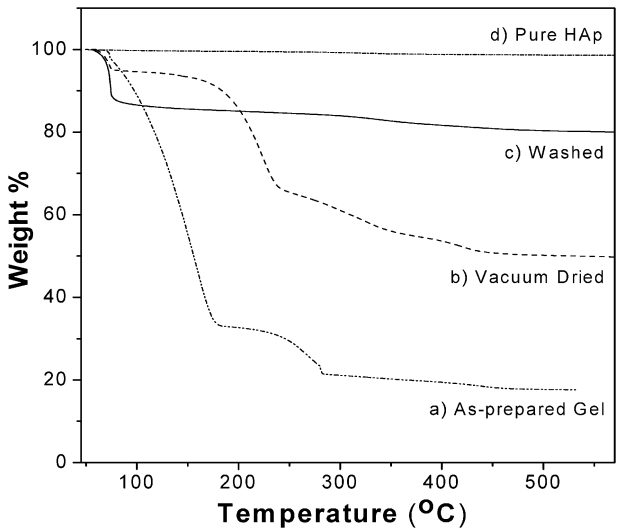

Fig. 3 TGA thermographs of (a) as-prepared HAp/polypeptide hydrogel, (b) vacuum dried HAp/polypeptide nanocomposite, (c) washed HAp/polypeptide nanocomposite and (d) pure HAp (Standard Reference Material® 2910).

completely by 500 °C. It is well established that HAp is thermally stable below 1000 °C[23] and there is almost no weight change for pure HAp between 50–570 °C, as shown in Fig. 3a. As a result, the HAp content for the CaP/polymer nanocomposite is determined to be approximately 53 wt% based on the dried sample at 175 °C. This is consistent with the theoretical weight ratio of HAp/block copolypeptide in the composite calculated from the amount of hydroxyapatite formed based on eqn (1).

NMR identification and quantification of phosphates

Fig. 4 shows direct-polarization (DP) and cross-polarization (CP) ^{31}P NMR spectra of the synthesized composite. The DP spectrum shows one dominant band, whose chemical shift (2.8 ppm) agrees with that of hydroxyapaptite,[62] though the linewidth is larger than for ideal HAp. The CP spectrum, which gives higher intensity to the phosphates close to protons, presents a different lineshape from DP, indicating the existence of more than one phosphate species. The broader base and significant intensity increase of the right shoulder of the CP spectrum suggests the presence of HPO_4^{2-} or of PO_4^{3-} hydrogen bonded to H_2O, in addition to apatitic PO_4^{3-}.

These assignments can be confirmed by recording ^{31}P DP spectra with 0 ms and 0.28 ms of recoupled ^{1}H–^{31}P dipolar dephasing, see Fig. S1a† (in the ESI), where a more distinct lineshape results from the different dephasing behavior of PO_4^{3-} and HPO_4^{2-}. Provided similar mobility, the signal of phosphates that are protonated or hydrogen bonded will dephase faster than that of nonprotonated ones. The dephasing curves obtained from the gated decoupling experiments are shown in Fig. S1b.† The difference in dephasing rate shows that there are two different phosphate components. One is not protonated, with very slow dephasing, and the other is monoprotonated or hydrogen-bonded to a proton.

Based on the differential dephasing of the phosphate signals, the DP/MAS spectrum can be deconvoluted into two different components as shown in Fig. 4a (dashed lines). The sharp component is PO_4^{3-} of hydroxyapatite, accounting for 68% of all phosphates, the broad one is HPO_4^{2-} or hydrogen-bonded PO_4^{3-}, accounting for 32%.

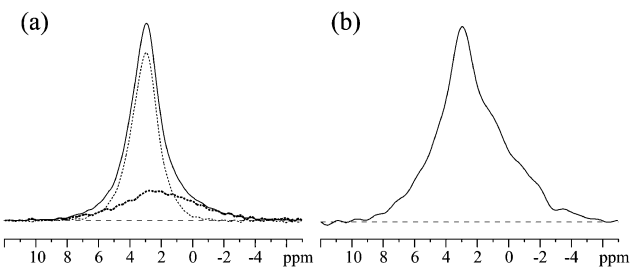

Fig. 4 ^{31}P NMR spectra of the synthesized composite. (a) Solid line: DP/MAS spectrum of all phosphates. Deconvolution based on ^{1}H–^{31}P dipolar dephasing is also shown; thin dashed line: PO_4^{3-}, 68%; thick dashed line: protonated or H-bonded phosphate, 32%. (b) CP/MAS with 1 ms cross polarization time.

NMR validation of nanocomposite formation

The one-dimensional spectra show that there are two types of phosphates present in the sample, but do not reveal whether they are part of nanocomposites. This information can be obtained by two-dimensional ^{1}H–^{31}P heteronuclear correlation NMR experiments with ^{1}H spin diffusion. Cross peaks between ^{1}H from the organic phase and ^{31}P from the inorganic phase are characteristic of nanocomposites.[29,63] For nanocomposites, the polymer proton peaks will show up within tens to hundreds of milliseconds. In Fig. 5, the spin diffusion from polymer protons to protons in the inorganic phase is indeed observed within 50 ms and equilibrium

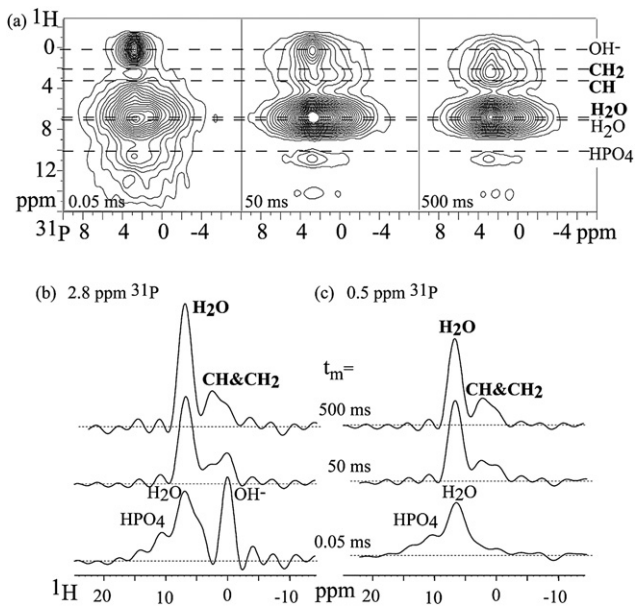

Fig. 5 (a) 2D ^{1}H–^{31}P HETCOR NMR spectra of the synthesized composite, with spin diffusion mixing times of 0.05 ms, 50 ms, and 500 ms. (b) and (c): Cross sections of the 2D spectra at 2.8 ppm and 0.5 ppm ^{31}P, respectively.

is reached within 500 ms. In samples with larger domains or for short spin diffusion times, the phosphates only "see" the protons close by, *i.e.* in the inorganic phase.

The series of ^{1}H–^{31}P correlation spectra in Fig. 5a were acquired with homonuclear decoupling in the ^{1}H dimension. Fig. 5b displays ^{1}H cross sections from the 2D spectra at 2.8 ppm ^{31}P, which demonstrate the spin diffusion process. On the time scale of 0.05 ms, phosphates only "see" OH^-, HPO_4^{2-} and H_2O protons. After 50 ms, the peak of a different H_2O species shows up, and within 500 ms, the CH and CH_2 proton signals come up along with a significant H_2O peak. The NH_4^+ peak of the polymer should also appear, but is overlapped by the dominant H_2O peak.[64] The completion of ^{1}H spin diffusion within 500 ms is signified by the disappearance of OH^- and HPO_4^{2-} proton peaks. This proves the formation of a nanocomposite. Fig. 5c reveals another ^{1}H environment associated with HPO_4^{2-} or $PO_4{\bullet}H_2O$. The appearance of the polymer proton peaks within 50 ms indicates fast spin diffusion, which is the evidence of nanocomposite formation. Therefore, both types of phosphates, hydroxyapatite PO_4^{3-} and HPO_4^{2-}, are part of a nanocomposite.

Fig. 6a shows a one-pulse ^{1}H spectrum with background suppression.[65] Several resolved peaks can be assigned according to their chemical shifts. H_2O and NH_3^+ peaks are centered at 7 ppm with a broad envelope; 7 ppm is the typical chemical shift of bound H_2O, while bulk water resonates at 5 ppm. After 18 hours of intensive vacuum drying of the samples at 105 °C in order to remove the mobile H_2O component, the 7 ppm peak shifted by 0.2 ppm and lost about 1/3 of its intensity, which means that the majority of H_2O in this composite is bound water. The broad peak of strongly bound water was observed at 0.05 ms in Fig. 6b, indicating that the strongly bound water has intimate contact with the inorganic phase. The sharp peak of the weakly bound H_2O became dominant after 50 ms spin diffusion, which means that the weakly bound water is also close to the inorganic phase. After extensive drying, the previously resolved CH and CH_2 polypeptide peaks became invisible in the one-pulse ^{1}H spectrum, see Fig. 6a (dashed line), which suggests that the removal of mobile H_2O reduces the mobility of the peptide. A band of NH_4^+, which happens to also resonate around 7 ppm, is present in the ^{1}H spectrum as a shoulder to the right of the intense water peak. ^{1}H T_1 measurements have shown that NH_4^+ has a longer T_1 than the components of the nanocomposite, proving that it forms a separate phase (NH_4NO_3).

The ^{1}H–^{31}P heteronuclear correlation experiments were also performed without ^{1}H homonuclear decoupling. Fig. 6 (b,c) displays cross sections from the 2D spectra (not shown) taken at 2.5 ppm and 0.5 ppm in the ^{31}P dimension. Without spin diffusion, the OH^- proton peak at 0.2 ppm in Fig. 6b confirms the peak assignment of hydroxyapatite in the ^{31}P spectra of Fig. 4. The strongly bound H_2O peak is not well resolved due to ^{1}H–^{1}H homonuclear coupling, while the weakly bound H_2O presents a sharp peak on the broad base of the strongly bound H_2O. The HPO_4^{2-} peak seen in Fig. 6c is not visible, likely also due to strong ^{1}H–^{1}H homonuclear coupling, which is common for interfacial HPO_4^{2-} species.

The 2D heteronuclear correlation experiments prove that both HPO_4^{2-} and hydroxyapatite are part of the nanocomposites, but do not establish whether they are in the same phase. This can be achieved instead by a one-dimensional ^{31}P spin diffusion experiment. If these two kinds of phosphates are in different phases, no ^{31}P spin diffusion between them will occur on the 10 s time scale. Conversely, fast spin diffusion from HPO_4^{2-} to hydroxyapatite proves that they are part of the same particle. After selection of HPO_4^{2-} ^{31}P magnetization by short cross polarization, narrowing of the line due to ^{31}P spin diffusion to PO_4^{3-} is actually observed within 1 s (Fig. 7), confirming that HPO_4^{2-} and hydroxyapatite are in the same phase and separated by less than 10 nm. Most likely, HPO_4^{2-} is at the interface of the inorganic phase with the polymer.

NMR characterization of the polypeptide phase in the nanocomposite

^{13}C NMR experiments have been carried out to study the conformation and mobility of polypeptide in the synthesized nanocomposite. The ^{13}C spectrum is shown in Fig. 8a (thin line). Peak assignments and literature values of solid-state ^{13}C NMR chemical shifts for α-helix and β-sheet conformations are marked above the spectra for ref. 66, 67. The chemical shifts indicate that the hydrophobic leucine domain is α-helical and that most lysine segments adopt a β-sheet conformation, while the rest is in

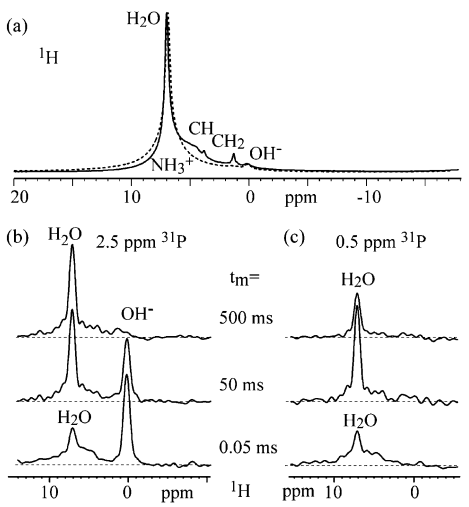

Fig. 6 ^{1}H spectra of the synthesized composite. (a) One-pulse ^{1}H spectrum of regular vacuum dried sample (solid line) and intensively dried sample (dashed line). (b, c) Cross sections from 2D "WISE" spectra at 2.5 ppm and 0.5 ppm ^{31}P, respectively, for a series of spin-diffusion times.

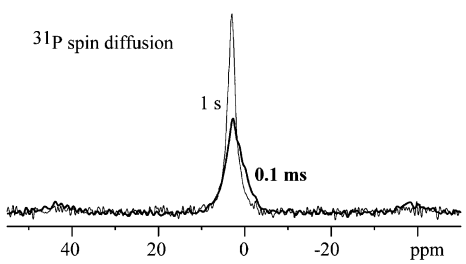

Fig. 7 ^{31}P NMR of the nanocomposite, with ^{31}P spin diffusion for 0.1 ms (thick line) and 1 s (thin line) after short (0.1 ms) cross polarization that selectively polarizes the protonated phosphates. MAS frequency: 6.5 kHz.

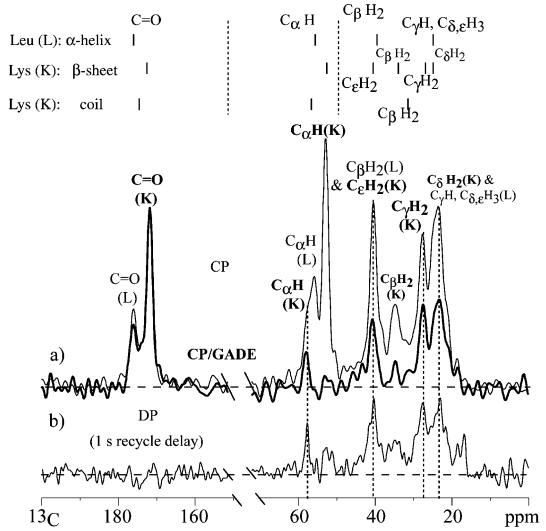

Fig. 8 Solid-state ^{13}C NMR spectra of $K_{170}L_{30}$ in the nanocomposite. (a) CP (thin line) and CP with 40 μs gated decoupling (thick line). (b) Direct polarization (DP) with 1 s recycle delay. Literature values of the solid-state ^{13}C chemical shifts are listed above the spectra for different peptide secondary structures.

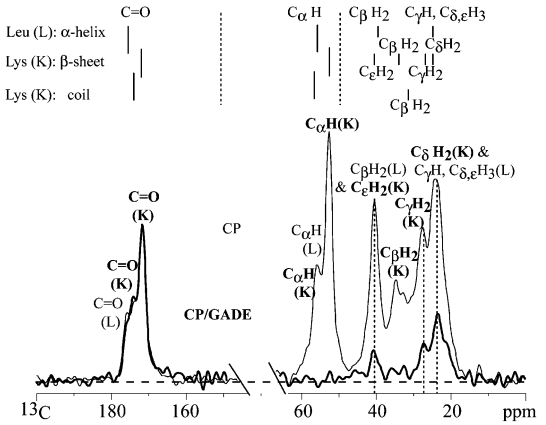

Fig. 9 Solid-state ^{13}C NMR spectra of the nanocomposite after intensive drying. CP (thin line) and CP with 40 μs gated decoupling (thick line).

a random-coil. This is consistent with the results of Deming and co-workers who have demonstrated that in hydrogels, 90% of the leucine domains of polypeptide $K_{160}L_{40}$ and $K_{180}L_{20}$ formed α-helices.[70] This shows that the α-helical structure of the poly-leucine domain[68] is retained even after the synthesis of the nanocomposite and vacuum drying. The peak intensities and the positions of the C_α and C_β signals are not consistent with the alternative assumption that the lysine segments are α-helical.

A corresponding CP ^{13}C NMR spectrum after 40 μs of gated decoupling was recorded in order to selectively detect mobile components of the polypeptide. High mobility will significantly reduce the C–H dipolar coupling, resulting in residual ^{13}C signals after gated decoupling. The resulting spectrum (thick line) in Fig. 8a indicates that the backbone of the polypeptide is rigid, since all the C_α signals for both leucine and lysine are completely dephased. The side chain carbons C_γ, C_δ and C_ε show significant residual intensity, which means that the side chains of the polypeptide are quite mobile.

Motions on the MHz scale generally induce fast T_1 relaxation, which enables another method to detect the mobile components. After direct polarization (DP) with a short recycle delay of 1 s, only signals of carbons with short T_1s are detected, see Fig. 8(b). Signals of all mobile carbons that are seen after gated decoupling (Fig. 8a, thick line) are also present in Fig. 8(b), confirming the conclusions about mobility. Besides, the absence of the carbonyl (C═O) and C_α signals in Fig. 8b confirms the rigidity of the polypeptide backbone.

However, the 70 : 30 signal intensity ratio of the rigid backbone carbons of lysine components to those of leucine in the CP spectrum of Fig. 8a does not match with the 85 : 15 stoichiometry of $K_{170}L_{30}$, which suggests some mobile lysine residues in the regularly vacuum dried sample are not detected in our CP spectra. In order to make these "invisible" components detectable, the intensively dried sample was studied. The ^{13}C spectra after CP and CP with gated decoupling are shown in Fig. 9. Changes in the CP spectrum upon intensive drying are indeed observed. First, C═O signals of random-coil lysine that do not show up in Fig. 8a, due to high mobility and resulting low CP efficiency, appear at 176 ppm after drying in Fig. 9. Second, the C_α peak of random-coil lysine that appears as a shoulder next to the C_α signal of α-helix leucine in Fig. 8a now shows up intensely in Fig. 9 (thin line) and overlaps with the C_α peak from leucine. Above all, the ratio of lysine to leucine backbone carbons obtained from the CP spectrum is approaching the theoretical ratio due to the contribution of the previously "invisible" random-coil lysine. Moreover, the CP spectrum (thin line) in Fig. 9 is less resolved than in Fig. 8a because of more peaks showing up and less dynamic conformational averaging. Furthermore, the reduced mobility is confirmed by the gated decoupling spectrum shown in Fig. 9 (thick line). The C_α peak of random-coil lysine vanishes, indicating that the backbone of random-coil lysine has become rigid after intensive drying. The decreased intensity of the residual signals in CP with gated decoupling in Fig. 8 compared to Fig. 9 confirms that the side chains are less mobile as well.

TEM of the nanocomposites

The TEM micrographs of the HAp crystals formed in the block copolypeptide gel and those obtained by direct synthesis from an aqueous solution are shown in Fig. 10. The HAp particles in the nanocomposite exhibit thin elongated plate-like morphology with a mean length of about 50–110 nm, width of 10–20 nm, and are about 3 nm thick (Fig. 10a). The elongated plate-like morphology of the HAp nanocrystals can also be seen from the STEM high angle annular dark field (HAADF) image in Fig. 10b. Appearance of needle-like morphology (Fig. 10a and b) is due to the on-edge viewing angle of the curled plate-like crystallites. Further, the morphology of HAp observed in the present study is quite similar to the apatite crystals found in human woven bone and mineralized dentin.[69,70] In general, bone mineral consists of plate-like crystals with average dimensions ~50–100 nm or more in length, ~25–50 nm in width, ~2–6 nm in thickness[60,69,71] and their small size is a crucial factor related to the solubility.[6] The SAED pattern of the as-prepared hydrogel sample given as an inset in Fig. 10a demonstrates well-defined

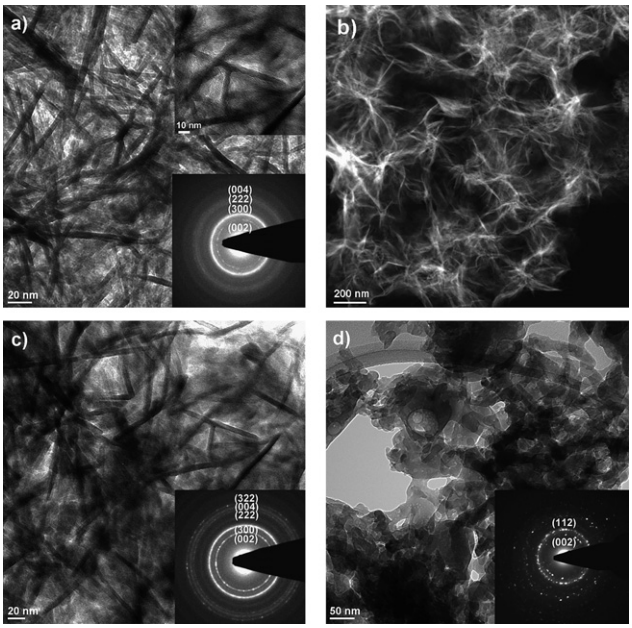

Fig. 10 TEM images and corresponding SAED patterns of HAp/polypeptide nanocomposite: (a) bright field, (b) STEM/HAADF, (c) washed HAp/polypeptide nanocomposite (after vacuum drying), (d) HAp nanocrystals obtained by direct synthesis from an aqueous solution in the absence of polymer.

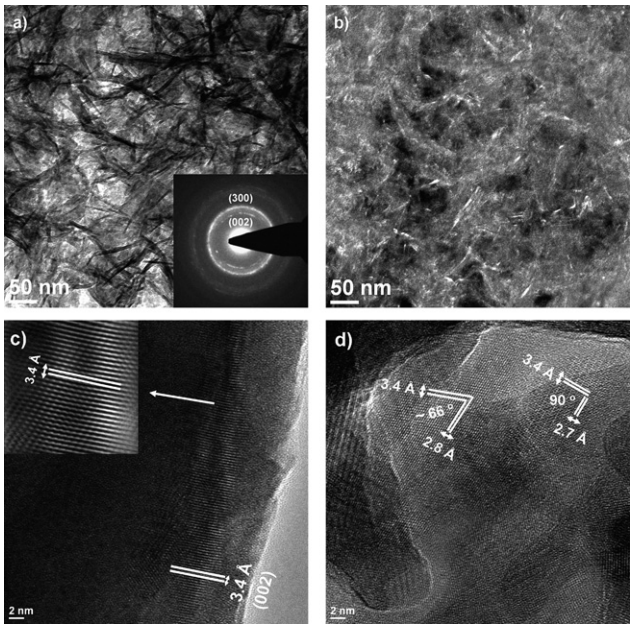

Fig. 11 (a) BF-TEM and (b) corresponding DF-TEM images of HAp/polypeptide nanocomposite, (c–d) HRTEM images of HAp/polypeptide nanocomposite. The lower inset in (a) shows the corresponding SEAD pattern and the upper inset in (c) shows the filtered inverse-FFT image of the indicated area.

broad ring patterns proving polycrystalline and nano-size nature of HAp phase. The observed diffraction rings can be indexed to HAp and these observations are in good agreement with the XRD and FTIR results. Moreover, Fig. 10c shows the bright-field TEM image of the washed sample (after vacuum drying) with the corresponding SAED pattern and it can be seen from the micrograph that the morphology of the HAp nanoparticles is very similar to that observed in the as-prepared hydrogel nanocomposite. In addition, it is also worth noting that the apatite crystals in the nanocomposites appear elongated plate-like, while the material prepared in the absence of polymer exhibit crystals with irregular shapes (Fig. 10d). Furthermore, the SAED pattern of HAp particles prepared in the absence of polymer shows many spots that do not form well defined rings (except from the (112) plane), indicating larger HAp crystals compared to the as-prepared nanocomposite sample.

Bright-field (BF) and dark-field (DF) transmission electron micrographs of the HAp/polypeptide nanocomposite taken from same area are displayed in Fig. 11a and 11b, respectively. The lower inset in Fig. 11a shows the corresponding SAED pattern with (300) and (002) diffraction rings of HAp. The DF-TEM image in Fig. 11b was obtained by isolating the HAp (002) diffraction in the nanocomposite. The mineral phase (HAp) appears as highlights in Fig. 11b, showing the HAp nanocrystals distribution in the amorphous polymer matrix. Moreover, the atomic calcium to phosphorus ratio of the inorganic phase was found to be 1.71 $\pm$ 0.07 by STEM-EDS measurements, which is in accordance with the stoichiometric value of pure HAp ($Ca_{10}(PO_4)_6(OH)_2$). The slight increase in Ca/P ratio of HAp over 1.67, the stoichiometric ratio, could be due to the carbonate substitution of the phosphate, consistent with FTIR results.

High-resolution TEM (HRTEM) analysis of the nanocomposites also confirmed the existence of HAp in the nanocomposite. The lattice fringe measurements from the HRTEM micrographs in Fig. 11c and 11d revealed *d* spacings of 3.44, 2.81, and 2.72 Å, corresponding to the (002), (211) and (300) HAp reflections, respectively. The upper inset in Fig. 11c demonstrates the filtered inverse-FFT image with (002) HAp planes from the indicated area of the HRTEM image. In addition, Fig. 11d shows the (002) and (211) HAp planes with an interplanar angle of ~66°, and the (002) and (300) HAp planes with an interplanar angle of 90°, which are consistent with the calculated values of HAp (JCPDS 9-432, a hexagonal unit cell (space group $P6_3/m$) with unit cell dimensions a = b = 9.418 Å and c = 6.884 Å). The HRTEM image of elongated plate-like nanocrystals in longitudinal sections (Fig. 11c) revealed a lattice spacing of 3.44 Å (corresponding to the interplanar spacing of (002) planes for hexagonal HAp), indicating that the growth of the plate-like nanocrystals occurs in the (001) direction. The intense (002) reflection in XRD (Fig. 1) also indicates that the c-axis is the preferred growth direction, which is similar to bone where nano-size apatite plate-like crystals associated with the collagen fibrils show strong preferred orientation in their c-axis.[1,54,69]

SAXS characterization

The nanocomposites were characterized with small angle X-ray scattering. The nanocomposites exhibited power law scattering (Fig. 12) similar to that observed in bone.[72,73] The characteristic length scale of the particles was found to be around 3 nm. In the SAXS data we observe signatures for the average size of the inorganic nanocrystals in the high Q region and power law scattering in the low Q region consistent[72,73] with the elongated

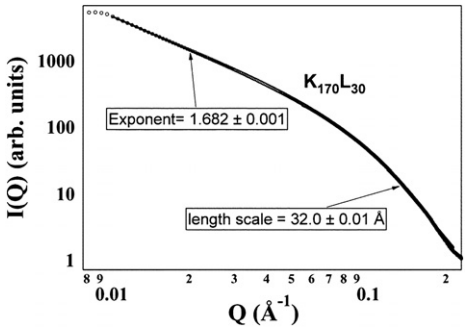

Fig. 12 SAXS of polypeptide nanocomposite. SAXS data were fitted using a combined equation consisting of an exponential and a power-law for the high Q region and power-law fitting was used for the low Q region.

particle morphologies observed in TEM. Further, modified Guinier analysis for the cross sectional dimensions shows the thickness of the particles to be around 3 nm, consistent with the TEM measurements.

Experimental

Materials and methods

All materials used were obtained from either Sigma Aldrich or Fisher Scientific and were of laboratory grade and purity.

Polypeptide synthesis

The polypeptide $K_{170}L_{30}$ was synthesized by the previously developed procedures.[68] Briefly, first N_{ε}-CBZ-L-lysine and L-leucine monomers were converted to α-aminoacid-N-carboxy-anhydrides (NCAs) to facilitate ring-opening polymerization. The NCA preparation was carried out with phosgene at 40 °C in dry tetrahydrofuran. The monomers were then reacted with $(PMe_3)_4Co$ initiator in THF and the polypeptide copolymerization was carried out under inert conditions at room temperature for 1 hour with sequential addition of the NCA monomers. The polymers were then dissolved in trifluoroacetic acid and deprotected by adding 33% HBr in acetic acid to solutions of copolypeptide in trifluoroacetic acid at 0 °C for 1 hour. The deprotected polymers were then dissolved in deionized water, dialyzed, and freeze dried. Polymer molecular weight and other chemical characteristics were determined by nuclear magnetic resonance (NMR), Fourier-transform infrared (FTIR) spectroscopy and gel permeation chromatography (GPC). FTIR was used to verify the consumption of the monomer and the formation of amide bonds in the polypeptide backbones. Tandem gel permeation chromatography/light scattering (GPC/LS) was performed at 60 °C using an SSI Accuflow Series III pump equipped with Wyatt DAWN EOS light scattering and Optilab rEX refractive index detectors. Separations were achieved using 10^5, 10^4, and 10^3 Å Phenomenex Phenogel 5 μm columns with 0.1 M LiBr in DMF as eluent and sample concentrations of 5 mg/mL. The deprotection of the polymers was then verified using ^{1}H NMR.

Block copolypeptide–hydroxyapatite nanocomposite synthesis

To prepare calcium phosphate (CaP)-polypeptide nanocomposite hydrogel samples, the following procedure was used: 0.11 g $K_{170}L_{30}$ was mixed with 1.5 mL 4.0 M $Ca(NO_3)_2 \cdot 4H_2O$ solution. To dissolve the polypeptide and form the hydrogel, the calcium containing polymer solution was kept at room temperature for two days. Then, 0.9 mL 4.0 M $(NH_4)_2HPO_4$ solution was added and aged at room temperature for an additional four days to form a CaP-hydrogel nanocomposite containing approximately 4.0 wt% polymer. In addition to the polypeptide and the inorganic phase, the gel contains mainly water along with some ammonium nitrate. The pH of the hydrogel sample was adjusted to ~8 from an initial pH of around 3 by adding NaOH solution. The formation of HAp in CaP/polymer hydrogel is believed to take place through the following simplified chemical reaction:

$$10Ca(NO_3)_2 + 6(NH_4)_2HPO_4 + 2H_2O \rightarrow Ca_{10}(PO_4)_6(OH)_2 + 12NH_4NO_3 + 8HNO_3 \quad (1)$$

Characterization

Calcium phosphate nanocomposite samples were analyzed by using techniques of X-ray diffraction (XRD), FTIR spectroscopy, thermogravimetric analysis (TGA), NMR, small angle X-ray scattering (SAXS), transmission electron microscopy (TEM), high resolution transmission electron microscopy (HRTEM), scanning transmission electron microscopy (STEM). Moreover, the atomic Ca/P ratio was also monitored by energy dispersive X-ray spectroscopy (EDS).

The structure and crystallinity of the as-prepared nanocomposite samples were investigated by a powder X-ray diffractometer (X'Pert PRO, PANalytical Inc., Westborough, MA, USA) using monochromatic CuKα radiation (λ = 0.15418 nm) and operating at 45 kV and 40 mA. The scanning rate was 0.008°/s with a step size of 0.017° over a range of $10° \leq 2\theta \leq 60°$. Scintag DMSNT search/match software and the ICDD 2007 database were used for the phase analysis.

Chemical analysis of the samples was carried out by a Bruker FTIR spectrometer (Bruker IFS-66v, Bruker Optics Inc., Billerica, MA, USA) over the range between 400–4000 cm^{-1} with a resolution of 4 cm^{-1} and averaging 32 scans. NMR studies (see below) require vaccum dried samples; therefore the XRD patterns of vaccum dried samples both before and after washing were obtained, to confirm the removal of ammonium nitrate during washing.

For the FTIR analysis of all the different samples mentioned above, the samples were pressed into KBr pellets containing approximately 1 wt% sample. The inorganic phase (HAp) content of the nanocomposites was estimated with a Perkin Elmer thermogravimetric analyzer (Perkin Elmer, TGA 7, Downers Grove IL, USA). Approximately 50 mg of the gel sample, the vaccum dried nanocomposite and the washed sample after vaccum drying, were heated to 50 °C under air flow conditions, held at this temperature for 1 min, then ramped to 120 °C at a rate of 5.0 °C/min, and at a rate of 10.0 °C/min to 550 °C. XRD patterns and FTIR spectra of the calcined samples, after being subject to thermogravimetric analysis, were also obtained.

Solid state NMR. Solid state NMR experiments were performed using a Bruker DSX400 spectrometer (Bruker-Biospin,

Rheinstetten, Germany) at 400 MHz for ^{1}H, 162 MHz for ^{31}P and 100 MHz for ^{13}C with a Bruker 4 mm magic-angle spinning double resonance probehead at ambient temperature. All samples were analyzed without washing, but were vacuum dried before NMR experiments because solid state NMR requires relatively dry samples to avoid power absorption by ionic conduction. The 90° pulse lengths were 4 μs for ^{1}H, 4.7 μs for ^{31}P and 4 μs for ^{13}C. All the ^{31}P and ^{1}H NMR experiments were carried out at a spinning speed of 6.5 kHz, while ^{13}C NMR experiments were at 4 kHz. ^{31}P direct polarization experiments, including those with gated recoupling, were performed with recycle delays of 100 s. ^{1}H–^{31}P correlation experiments without ^{1}H homonuclear decoupling, using the wideline separation (WISE) NMR pulse sequence with hypercomplex data acquisition, were carried out with 256 20 μs t_1 increments and 2 s recycle delays. 2D ^{1}H–^{31}P heteronuclear correlation (HetCor) NMR experiments were carried out with 100 44 μs t_1 increments of FSLG homonuclear decoupling and 2 s recycle delays. Lee-Goldburg cross polarization (LGCP) was used for polarization transfer from ^{1}H to ^{31}P in both "WISE" [74] and HetCor experiments with contact times of 0.7 ms and 0.5 ms, respectively. 1D ^{31}P spin diffusion experiments after 0.1 ms of cross polarization were accomplished with spin diffusion times of 0.1, 0.5, 1, 5, 10, 50, 100, 500 ms, and 1 s. ^{13}C cross polarization and cross polarization with gated decoupling of 40 μs were used to detect the mobile components in the polypeptide phase. These ^{13}C NMR experiments were carried out with recycle delays of 2 s and 45 056 scans. ^{1}H one-pulse NMR spectrum was obtained with 3.8 μs ^{1}H 90° pulse and background suppression. Two-pulse phase-modulation (TPPM) was used for heteronuclear dipolar decoupling in all these experiments. The proton peak at 0.18 ppm and ^{31}P peak at 2.8 ppm of NIST hydroxyapatite were used as secondary references to calibrate the ^{1}H and ^{31}P chemical shifts, respectively. The C=O carbon peak at 176.49 ppm of 25% ^{13}C labeled α-glycine was used for ^{13}C chemical shift calibration.

Electron microscopy. STEM, HRTEM, Selected-Area Electron Diffraction (SAED), and EDS studies were performed with a FEI-Tecnai G^2 F20 (FEI Inc., Hillsboro, OR, USA) scanning transmission electron microscope equipped with EDS (EDAX Inc., Mahwah, NJ, USA) using a CCD camera and Digital Micrograph Software (Gatan, Pleasanton, CA, USA). For the TEM analysis, a small amount of HAp/copolypetide hydrogel sample was placed onto a Formvar-coated copper grid and a negative contrast stain consisting of 1.0% ammonium molybdate at pH ~8 was applied. After applying the stain, the excess solution was wicked away and the sample was allowed to dry.

Small angle X-ray scattering (SAXS). The structural order and length scale of the polymer gel structure were estimated by SAXS. Scattering measurements were performed at the 12-ID beam line at the Advanced Photon Source at Argonne National Laboratory. Gel nanocomposite samples were sandwiched between Kapton tapes, and placed 2 m from the detector to investigate the nanocomposite structure and templating properties of the polypeptide. A 15 × 15 cm detector was used to measure the scattered intensity and the transmitted intensity was measured using a photodiode. The beam energy used for the analysis is 12 keV ($\lambda = 1.035$ Å) and the data were collected at 1 s exposure, and the collected 2D data were corrected, azimuthally averaged.

Conclusions

HAp/copolypeptide nanocomposites were obtained *via* a simple co-precipitation method at room temperature with the block copolypeptides serving as the organic template, similar to natural bone that is a complex inorganic (HAp) –organic (collagen) nanocomposite material. This method allows for simultaneous formation of the self-assembled block copolypeptide gel and of the inorganic phase, thereby enabling formation of a self-assembled nanocomposite. Block copolypeptide templates that form gels at very low weight fractions (0.5–4 wt%) compared to previously investigated synthetic block copolymers, allow for inorganic content in the nanocomposites of over 50 wt%, more closely approaching the inorganic content seen in natural bone. Previous research[75,76] has shown that the increase of HAp content will result in an increase in the elastic modulus but a decrease in the tensile strength and ductility. A good compromise of these mechanical properties can be obtained in the composite of HAp weight fraction of 60–70%, *i.e.* the composition of native bone. As mentioned earlier, most of the synthetic biomineralization efforts have yielded only about 30 wt% inorganic fraction. Therefore, the present work is unique in that we have been able to increase the inorganic weight fraction to over 50%, more closely approaching the inorganic content in bone. Solid state NMR studies proved the existence of a nanocomposite, with the inorganic phase composed mainly of hydroxyapatite but also HPO_4^{2-}. The morphology of the inorganic nanoparticles is very different from that obtained by precipitation in the absence of the block copolypeptides. The data obtained from XRD, FTIR, S/TEM, SAED, HRTEM, EDS, solid state NMR and small angle scattering studies are consistent and lead us to the conclusion that the inorganic phase present in the nanocomposite is carbonated HAp of nano-scale dimensions, with elongated plate-like morphology very similar to the mineral phase of bone. Overall, this approach allows us to synthesize self-assembled calcium phosphate nanocomposites using organic templates, which could have a potential applications in soft tissue repair.

Acknowledgements

This work was supported by the US Department of Energy under contract number DE-AC02-07CH11358. This work benefited from the use of APS and the IPNS, funded by the US DOE, Office of Science, Office of Basic Energy Science under contract no DE-AC02-06CH11357. Supporting Information is available online from The Royal Society of Chemistry or from the authors.

References

1 S. V. Dorozhkin and M. Epple, *Angew. Chem., Int. Ed.*, 2002, **41**, 3130–3146.
2 R. K. Roeder, G. L. Converse, R. J. Kane and W. Yue, *JOM*, 2008, **60**, 38–45.
3 M. Vallet-Regi, *Dalton Trans.*, 2006, 5211–5220.
4 A. Bigi, E. Boanini, S. Panzavolta, N. Roveri and K. Rubini, *J. Biomed. Mater. Res.*, 2002, **59**, 709–715.

5 J. Y. Rho, L. Kuhn-Spearing and P. Zioupos, *Medical engineering & physics*, 1998, **20**, 92–102.
6 M. Vallet-Regi and J. M. Gonzalez-Calbet, *Prog. Solid State Chem.*, 2004, **32**, 1–31.
7 K. S. Anseth, V. R. Shastri, C. T. Laurencin and R. Langer, *Abstracts of Papers of the American Chemical Society*, 1996, **211**, 228.
8 Z. Li, Y. Li, A. Yang, X. Peng, X. Wang and Z. Xiang, *J. Mater. Sci.: Mater. Med.*, 2005, **16**, 213–219.
9 S. Mann, *Biomineralization: Principles and Concepts in Bioinorganic Materials Chemistry*, 2001.
10 Z. Amjad, *Calcium Phosphates In Biological And Industrial Systems*, Kluwer Academic Publishers, Boston, 1998.
11 A. Sinha, S. Nayar, A. Agrawal, D. Bhattacharyya and P. Ramachandrarao, *J. Am. Ceram. Soc.*, 2003, **86**, 357–359.
12 J. Song, V. Malathong and C. R. Bertozzi, *J. Am. Chem. Soc.*, 2005, **127**, 3366–3372.
13 N. Spanos, V. Deimede and P. G. Koutsoukos, *Biomaterials*, 2002, **23**, 947–953.
14 T. Taguchi, A. Kishida and M. Akashi, *J. Biomater. Sci., Polym. Ed.*, 1999, **10**, 795–804.
15 W. Tjandra, P. Ravi, J. Yao and K. C. Tam, *Nanotechnology*, 2006, **17**, 5988–5994.
16 Y. F. Zhao and J. Ma, *Microporous Mesoporous Mater.*, 2005, **87**, 110–117.
17 N. Degirmenbasi, D. M. Kalyon and E. Birinci, *Colloids Surf., B*, 2006, **48**, 42–49.
18 L. F. Sukhodub, C. Moseke, L. B. Sukhodub, B. Sulkio-Cleff, V. Y. Maleev, M. A. Semenov, E. G. Bereznyak and T. V. Bolbukh, *J. Mol. Struct.*, 2004, **704**, 53–58.
19 M. Kikuchi, S. Itoh, S. Ichinose, K. Shinomiya and J. Tanaka, *Biomaterials*, 2001, **22**, 1705–1711.
20 F. Z. Cui, Y. Wang, Q. Cai and W. Zhang, *J. Mater. Chem.*, 2008, **18**, 3835–3840.
21 I. Manjubala, S. Scheler, J. Bossert and D. Jandt Klaus, *Acta Biomater.*, 2006, **2**, 75–84.
22 V. M. Rusu, C.-H. Ng, M. Wilke, B. Tiersch, P. Fratzl and M. G. Peter, *Biomaterials*, 2005, **26**, 5414–5426.
23 L. Wang and C. Li, *Carbohydr. Polym.*, 2007, **68**, 740–745.
24 S. A. Hutchens, R. S. Benson, B. R. Evans, H. M. O'Neill and C. J. Rawn, *Biomaterials*, 2006, **27**, 4661–4670.
25 L. Hong, Y. L. Wang, S. R. Jia, Y. Huang, C. Gao and Y. Z. Wan, *Mater. Lett.*, 2006, **60**, 1710–1713.
26 P. Cromme, C. Zollfrank, L. Mueller, F. A. Mueller and P. Greil, *Materials Science & Engineering, C: Biomimetic and Supramolecular Systems*, 2007, **27**, 1–7.
27 K. R. Mohamed and A. A. Mostafa, *Materials Science & Engineering, C: Materials for Biological Applications*, 2008, **28**, 1087–1099.
28 M. C. Chang, C.-C. Ko and W. H. Douglas, *Biomaterials*, 2003, **24**, 3087–3094.
29 D. Enlow, A. Rawal, M. Kanapathipillai, K. Schmidt-Rohr, S. Mallapragada, C. T. Lo, P. Thiyagarajan and M. Akinc, *J. Mater. Chem.*, 2007, **17**, 1570–1578.
30 M. Kanapathipillai, Y. Yusufoglu, A. Rawal, Y. Y. Hu, C. T. Lo, P. Thiyagarajan, Y. E. Kalay, M. Akinc, S. Mallapragada and K. Schmidt-Rohr, *Chem. Mater.*, 2008, **20**, 5922–5932.
31 Y. Yusufoglu, Y. Y. Hu, M. Kanapathipillai, K. Matthew, Y. E. Kalay, P. Thiyagarajan, M. Akinc, K. Schmidt-Rohr and S. Mallapragada, *J. Mater. Res.*, 2008, **23**, 3196–3212.
32 L. Wang, Y. Li and C. Li, *J. Nanopart. Res.*, 2009, **11**, 691–699.
33 S.-C. Liou, S.-Y. Chen and D.-M. Liu, *Biomaterials*, 2003, **24**, 3981–3988.
34 J. N. Cha, G. D. Stucky, D. E. Morse and T. J. Deming, *Nature*, 2000, **403**, 289–292.
35 L. E. Euliss, S. G. Grancharov, S. O'Brien, T. J. Deming, G. D. Stucky, C. B. Murray and G. A. Held, *Nano Lett.*, 2003, **3**, 1489–1493.
36 V. Krikorian, M. Kurian, M. E. Glavin, A. P. Nowak, T. J. Deming and D. J. Pochan, *J. Polym. Sci., Part B: Polym. Phys.*, 2002, **40**, 2579–2586.
37 M. M. Tomczak, D. D. Glawe, L. F. Drummy, C. G. Lawrence, M. O. Stone, C. C. Perry, D. J. Pochan, T. J. Deming and R. R. Naik, *J. Am. Chem. Soc.*, 2005, **127**, 12577–12582.
38 K. Donadel, M. C. M. Laranjeira, V. L. Goncalves, V. T. Favere, J. C. de Lima and L. H. M. Prates, *J. Am. Ceram. Soc.*, 2005, **88**, 2230–2235.
39 K. Kandori, N. Horigami, A. Yasukawa and T. Ishikawa, *J. Am. Ceram. Soc.*, 1997, **80**, 1157–1164.
40 A. Lopez-Macipe, J. Gomez-Morales and R. Rodriguez-Clemente, *Adv. Mater.*, 1998, **10**, 49–53.
41 Y. Yusufoglu and M. Akinc, *J. Am. Ceram. Soc.*, 2008, **91**, 3147.
42 M. Aizawa, A. E. Porter, S. M. Best and W. Bonfield, *Biomaterials*, 2005, **26**, 3427–3433.
43 M. Aizawa, H. Ueno, K. Itatani and I. Okada, *J. Eur. Ceram. Soc.*, 2006, **26**, 501–507.
44 M. Kinoshita, K. Itatani, S. Nakamura and A. Kishioka, *Gypsum Lime*, 1990, **227**, 207–215.
45 A. Barroug, J. Lemaitre and P. G. Rouxhet, *J. Alloys Compd.*, 1992, **188**, 152–156.
46 K. Ishikawa, E. D. Eanes and M. S. Tung, *J. Dent. Res.*, 1994, **73**, 1462–1469.
47 A. Slosarczyk, Z. Paszkiewicz and C. Paluszkiewicz, *J. Mol. Struct.*, 2005, **744–747**, 657–661.
48 T. Iizuka and A. Nozuma, *J. Ceram. Soc. Japan*, 1998, **106**, 820–823.
49 R. Z. LeGeros, J. P. LeGeros, O. R. Trautz and W. P. Shirra, *Adv. X-Ray Anal.*, 1971, **14**, 57–66.
50 E. A. P. De Maeyer, R. M. H. Verbeeck and D. E. Naessens, *Inorg. Chem.*, 1993, **32**, 5709–5714.
51 J. Liu, X. Ye, H. Wang, M. Zhu, B. Wang and H. Yan, *Ceram. Int.*, 2003, **29**, 629–633.
52 H. Monma and T. Kamiya, *J. Mater. Sci.*, 1987, **22**, 4247–4250.
53 J. C. Elliott, *Structure and Chemistry of the Apatites and Other Calcium Orthophosphates*, Elsevier, Amsterdam, 1994.
54 S. N. Danilchenko, C. Moseke, L. F. Sukhodub and B. Sulkio-Cleff, *Cryst. Res. Technol.*, 2004, **39**, 71–77.
55 S. Liao, F. Watari, M. Uo, S. Ohkawa, K. Tamura, W. Wang and F. Cui, *J. Biomed. Mater. Res., Part B*, 2005, **74b**, 817–821.
56 J. P. Coates, *Appl. Spectrosc. Rev.*, 1996, **31**, 179–192.
57 G. Xu, I. A. Aksay and J. T. Groves, *J. Am. Chem. Soc.*, 2001, **123**, 2196–2203.
58 K. Sato, *Top. Curr. Chem.*, 2007, **270**, 127–153.
59 R. Murugan, S. Ramakrishna and K. P. Rao, *Mater. Lett.*, 2006, **60**, 2844–2847.
60 E. Sachlos, D. Gotora and J. T. Czernuszka, *Tissue Engineering*, 2006, **12**, 2479–2487.
61 N. A. Zakharov, Z. A. Ezhova, E. M. Koval, V. T. Kalinnikov and A. E. Chalykh, *Inorg. Mater.*, 2005, **41**, 509–515.
62 W. P. Rothwell, J. S. Waugh and J. P. Yesinowski, *J. Am. Chem. Soc.*, 1980, **102**, 2637–2643.
63 S. S. Hou, F. L. Beyer and K. Schmidt-Rohr, *Solid State Nucl. Magn. Reson.*, 2002, **22**, 110–127.
64 K. Wuthrich, *NMR of Proteins and Nucleic Acids*, 1986.
65 Q. Chen, S. S. Hou and K. Schmidt-Rohr, *Solid State Nucl. Magn. Reson.*, 2004, **26**, 11–15.
66 Y. Wang, *J. Biomol. NMR*, 2004, **30**, 233–244.
67 C. Ye, R. Fu, J. Hu, L. Hou and S. Ding, *Magn. Reson. Chem.*, 1993, **31**, 699–704.
68 A. P. Nowak, V. Breedveld, L. Pakstis, B. Ozbas, D. J. Pine, D. Pochan and T. J. Deming, *Nature*, 2002, **417**, 424–428.
69 X. Su, K. Sun, F. Z. Cui and W. J. Landis, *Bone (New York, NY, United States)*, 2003, **32**, 150–162.
70 P. Houlle, J. C. Voegel, P. Schultz, P. Steuer and F. J. G. Cuisinier, *J. Dent. Res.*, 1997, **76**, 895–904.
71 W. J. Landis, M. J. Song, A. Leith, L. McEwen and B. F. McEwen, *J. Struct. Biol.*, 1993, **110**, 39–54.
72 P. Fratzl, N. Fratzl-Zelma, K. Klaushofer, G. Vogl and K. Koller, *Calcif. Tissue Int.*, 1991, **48**, 407–413.
73 P. Fratzl, M. Groschner, G. Vogl, H. Plenk, J. Eschberger, N. Fratzl-Zelman, K. Koller and K. Klaushofer, *J. Bone Mineral Res.*, 1992, **7**, 329–334.
74 K. Schmidt-Rohr, J. Clauss and H. W. Spiess, *Macromolecules*, 1992, **25**, 3273–3277.
75 L. Fang, L. Yang and P. Gao, *Key Eng. Mater.*, 2007, **10**, 334–335.
76 S. Mollazadeh, J. Javadpour and A. Khavandi, *Adv. Appl. Ceram.*, 2007, **106**, 165–170.
77 R. Gonzalez-McQuire, J.-Y. Chane-Ching, E. Vignaud, A. Lebugle and S. Mann, *J. Mater. Chem.*, 2004, **14**, 2277–2281.
78 J. D. Hartgerink, E. Beniash and S. I. Stupp, *Science*, 2001, **294**, 1684–1688.
79 A. D. Roddick-Lanzilotta and A. J. McQuillan, *J. Colloid Interface Sci.*, 1999, **217**, 194–202.
80 M. Rozenberg and G. Shoham, *Biophys. Chem.*, 2007, **125**, 166–171.

